JOURNAL OF AIRCRAFT
Vol. 42, No. 5, September–October 2005

Modified Shear-Stress Transport Turbulence Model for Supersonic Flows

Sang Dug Kim* and Dong Joo Song†
Yeungnam University, Gyeongsangbuk-do, 712-749, Republic of Korea

The shear-stress transport turbulence model of Menter was derived to predict an accurate separated flow in the adverse pressure gradient flowfield, but it has sometimes failed to analyze these regions due to the strong shock/boundary-layer interaction. The modification of the shear-stress transport turbulence model adopted the shear strain rate instead of the vorticity as a limitation of the shear stress. The modified shear-stress transport turbulence model was applied to simulate supersonic compression corner flows including strong shock/boundary-layer interactions, and its performance in predicting the wall pressure distribution and the skin-friction coefficient was evaluated. The pressure distributions on the wall surface predicted by the modified shear-stress transport turbulence model showed an agreement with the experimental data in a transonic axisymmetric bump flow with the weak shock/boundary-layer interaction. In the cases of the 20- and 24-deg compression corner flows with strong shock/boundary-layer interactions, the modified shear-stress transport turbulence model yielded a more accurate prediction of the shock location and the wall pressure distribution and it also produced the more reasonable mean velocity profiles and skin-friction coefficient distribution in the redevelopment region as compared to the shear-stress transport turbulence model.

Nomenclature

A	=	Jacobian matrix
a	=	sonic speed
C_f	=	skin-friction coefficient, $2\tau_w/\rho_\infty u_\infty^2$
c	=	chord of bump
E	=	volumetric total energy, $e + \rho(u^2 + v^2)/2$
e	=	volumetric internal energy, $p/(\gamma - 1)$
$\boldsymbol{F}, \boldsymbol{G}$	=	flux vectors
k	=	turbulent kinetic energy
Pr	=	Prandtl number
p	=	static pressure
q	=	conservative variables
$\tilde{q}$	=	primitive variables
$\tilde{q}$	=	characteristic variables
Re	=	Reynolds number
$\boldsymbol{S}_0$	=	source term vector
u, v	=	Cartesian velocity components
u_τ	=	friction velocity
δ	=	boundary-layer thickness
γ	=	specific heat ratio
κ	=	von Kármán constant
μ	=	molecular viscosity
μ_t	=	turbulent eddy viscosity
ν	=	kinematic viscosity
σ_k, σ_ω	=	turbulent Prandtl numbers for k and ω
ω	=	dissipation rate of turbulent kinetic energy

Subscripts

t	=	turbulence quantity
w	=	quantity at the wall
0	=	quantity at the inlet, stagnation value
∞	=	freestream quantity

Received 17 April 2004; revision received 22 October 2004; accepted for publication 26 October 2004.

*Visiting Professor, School of Mechanical Engineering, Korea 214-1, Dae-dong, Gyeongsan-si; sangkim@yu.ac.kr.

†Professor, School of Mechanical Engineering, Korea 214-1, Dae-dong, Gyeongsan-si.

I. Introduction

THE phenomena of shock/boundary-layer interaction (SBLI), subsequent separation, and unsteadiness are the most interesting and difficult problems to predict in aerodynamics. Because of the complex nature of the flowfield, even though the overall flowfield can be reasonably predicted in supersonic flows with strong interactions between the shock and turbulent boundary layer, the prediction of the proper extent and size of the flow separation region and the accurate skin-friction coefficient is extremely difficult.[1–5] A lot of experimental, analytical, and numerical studies have been conducted to better understand the physics of SBLI and to evolve accurate prediction methods because these phenomena are easily found in many practical areas of external aerodynamics, as well as fluid mechanics, and directly effect the performance of engine inlets, compressors, and turbines in high-speed aircraft. A precise prediction of the SBLI will not only enhance the performance of an engine's components, but also may help establish a significant reduction in design and fabrication costs.

When a supersonic flow over a compression ramp, which is typical of a deflected control surface of a high-speed aircraft, is considered, shock waves occur at the corner and yield a rise in pressure. This adverse pressure gradient becomes stronger as the deflection angle of the ramp and Mach number increases, eventually producing flow separation, which may incur oscillating shock and unsteady pressure loads on the structure body.

A series of experimental studies on several compression corners were undertaken by Settles et al.[1] Those experiments were conducted at a freestream Mach number of 2.85 and at ramp angles of 8, 16, 20, and 24 deg and provided details of the flowfield with SBLIs. They are now used in the present computational investigation for assessment of turbulent models.

One of the major elements used to obtain an accurate prediction is the excellent performance of the turbulence model. An algebraic turbulence model was adopted for compressible Navier–Stokes codes because it is easy to implement and it requires minimum computer time and storage. Baldwin and Lomax[6] proposed an algebraic eddy-viscosity model that does not require the determination of the boundary-layer edge because it employs the vorticity. Visbal and Knight[2] carried out a comparative study on a modified model for

upstream history effect and the original Baldwin–Lomax model for the supersonic compression corner problem. However, these models failed to predict the rapid recovery of boundary layer downstream of a reattachment point.

Two-equation turbulence models have the capability of predicting more complex flows than zero; and one-equation models because both velocity and length scales are solved locally. Two-equation models, however, are based on the assumption that the Boussinesq approximation is valid and that the turbulence is isotropic. The low Reynolds number k–ε formulation of two-equation turbulence models has been widely adopted in practical engineering problems due to its robustness. The k–ω model of Wilcox[3] was proposed to overcome disadvantages of the k–ε model, which fails to reproduce correctly the effects of the solid wall boundary on turbulence. Wilcox tested several low Reynolds number k–ε models and the k–ω model by computing the boundary layer with various pressure gradients. The k–ω model predicted the skin-friction coefficient to be more accurate for strong adverse pressure gradient flows. For the k–ω model, however, the freestream value of ω produced some effects on boundary layers, although the k–ε model is not sensitive to the freestream value of ε, as discussed by Menter.[7]

A turbulence model, called baseline (BSL) model, was proposed by Menter,[8] which combined the k–ω and k–ε models by using a switching function. This model is identical to the k–ε model in terms of the free shear layer and is also insensitive to freestream values of ω. Another proposed version of the model is called the shear-stress transport (SST) model, which can account for the transport of the turbulent shear stress in turbulent boundary layers. This model was derived through the use of Bradshaw's assumption that the principal shear stress is proportional to the turbulent kinetic energy. The predictions of the SST model show an agreement with the experimental data for adverse pressure gradient boundary-layer flow, when the flow has a weak SBLI. The SST model, however, has sometimes failed to predict the flowfield with a strong SBLI. Forsythe et al.[4] investigated the six popular turbulence models, including the SST model for supersonic compression ramp flow. His investigation showed that all models studied, with and without compressibility modifications, failured to predict the shock position and the rapid recovery of the velocity profile downstream of the shock, as well as overpredicted the wall pressure rise within the separation zone. The primary purpose of this work is to find a possible improvement of the assumption implied in the SST model for better prediction in strong SBLI.

In the meantime, the finite-difference method based on the upwind scheme has been developed by various researchers. The upwind method is appropriate due to its robustness in capturing the shock wave in the transonic/supersonic flow. Classical upwind schemes can roughly be divided into two categories: flux vector splitting schemes (Steger-Warming[9] and Van Leer[10]) and flux difference splitting schemes (Godunov,[11] Roe,[12] and Osher[13]). In the original Godunov scheme, the local Riemann problem is solved exactly; however, Roe and Osher used approximate Riemann solvers instead. Among the upwind flux difference splitting Navier–Stokes methods, Lombard et al.[14] solved two-/three-dimensional complex high-speed flow quite efficiently with reasonable accuracy using the conservative supra characteristic method (CSCM). The CSCM-type upwind flux difference splitting scheme has the merits of the upwind scheme, the ease of applying characteristic boundary conditions, and the robust flow solver. Kim et al.[15] have successfully studied the usage of the Kolmogorov velocity scale instead of the conventional velocity scale in modifying a turbulence model for a supersonic flow, and Song et al.[16] have shown the off-design performance of centrifugal compressor diffusers with various mass flow rates using a CSCM-type upwind method.

In this work, we used the CSCM upwind Navier–Stokes code with three, two-equation turbulence models, Menter's BSL and SST models and the modified SST(MSST) model proposed here, to appraise their performances in predicting compression corner flows with strong SBLIs.

II. Governing Equations and Turbulence Closure

A. BSL Model

The BSL model was proposed to keep the best features of both models, that is, to retain the robust and accurate formulation of the k–ω model in the near wall region and to take advantage of the insensitive feature based on the freestream values of the k–ε model. The function $\boldsymbol{F}_1$ was designed to switch from the k–ω model for the wall surface to the k–ε model for the free shear flow, and the blending is to take place in the wake region of the boundary layer. The two-dimensional Reynolds averaged Navier–Stokes equation with Menter's BSL model can be written as

$$\frac{\partial q}{\partial t}+\frac{\partial \boldsymbol{F}}{\partial x}+\frac{\partial \boldsymbol{G}}{\partial y}=\frac{\partial \boldsymbol{F}_v}{\partial x}+\frac{\partial \boldsymbol{G}_v}{\partial y}+\boldsymbol{S}_0 \tag{1}$$

with

$$q=\begin{bmatrix}\rho\\ \rho u\\ \rho v\\ E\\ \rho k\\ \rho\omega\end{bmatrix},\qquad \boldsymbol{F}=\begin{bmatrix}\rho u\\ \rho u^2+p\\ \rho uv\\ u(E+p)\\ \rho uk\\ \rho u\omega\end{bmatrix},\qquad \boldsymbol{G}=\begin{bmatrix}\rho u\\ \rho uv\\ \rho v^2+p\\ v(E+p)\\ \rho uk\\ \rho u\omega\end{bmatrix} \tag{2}$$

$$\boldsymbol{F}_v=\begin{bmatrix}0\\ \tau_{xx}\\ \tau_{xy}\\ u\tau_{xx}+v\tau_{xy}-Q_x\\ (\mu+\sigma_k\mu_t)\dfrac{\partial k}{\partial x}\\ (\mu+\sigma_\omega\mu_t)\dfrac{\partial \omega}{\partial x}\end{bmatrix},\qquad \boldsymbol{G}_v=\begin{bmatrix}0\\ \tau_{yx}\\ \tau_{yy}\\ u\tau_{yx}+v\tau_{yy}-Q_y\\ (\mu+\sigma_k\mu_t)\dfrac{\partial k}{\partial y}\\ (\mu+\sigma_\omega\mu_t)\dfrac{\partial \omega}{\partial y}\end{bmatrix} \tag{3}$$

The effective stress tensor and the effective heat flux vector are given by

$$\tau_{ij}=(\mu+\mu_t)\left[\left(\frac{\partial u_i}{\partial x_j}+\frac{\partial u_j}{\partial x_i}\right)-\frac{2}{3}\delta_{ij}\frac{\partial u_m}{\partial x_m}\right]-\delta_{ij}\rho k \tag{4}$$

$$\boldsymbol{Q}_i=-C_p\left(\frac{\mu}{Pr_l}+\frac{\mu_t}{Pr_t}\right)\frac{\partial T}{\partial x_i} \tag{5}$$

Furthermore, the source term vector is given by

$$\boldsymbol{S}_0=\begin{bmatrix}0\\ 0\\ 0\\ 0\\ P_k-\beta^*\rho\omega k\\ \dfrac{\gamma\rho}{\mu_t}P_k-\beta\rho\omega^2+2\rho(1-\boldsymbol{F}_1)\sigma_{\omega 2}\dfrac{1}{\omega}\dfrac{\partial k}{\partial x_j}\dfrac{\partial \omega}{\partial x_j}\end{bmatrix} \tag{6}$$

where turbulence kinetic energy production is

$$P=\left[\mu_t\left(\frac{\partial u_i}{\partial x_j}+\frac{\partial u_j}{\partial x_i}-\frac{2}{3}\frac{\partial u_k}{\partial x_k}\delta_{ij}\right)-\frac{2}{3}\rho k\delta_{ij}\right]\frac{\partial u_i}{\partial x_j} \tag{7}$$

To compute the switching function $\boldsymbol{F}_1$,

$$\arg_1=\min\left[\max\left(\frac{\sqrt{k}}{0.09wy};\frac{500\mu}{\rho\omega y^2}\right);\frac{4\rho\sigma_{\omega 2}k}{CD_{k\omega}y^2}\right] \tag{8}$$

$$CD_{k\omega}=\max\left(2\rho\sigma_{\omega 2}\frac{1}{\omega}\frac{\partial k}{\partial x_j}\frac{\partial \omega}{\partial x_j};10^{-20}\right) \tag{9}$$

$$F_1 = \tanh\left(\arg_1^4\right) \tag{10}$$

The switching function is designed to be in the near-wall region and zero away from the surface, which determines the value of the model constants. If ϕ_1 represents a constant of the k–ω model, and ϕ_2 represents the same constant for the k–ε model, the new model constants are expressed by ϕ:

$$\phi = \boldsymbol{F}_1\phi_1 + (1 - \boldsymbol{F}_1)\phi_2 \tag{11}$$

The following two sets of model constants are used:

Set 1 (ϕ_1):

$$\sigma_{k_1} = 0.5, \qquad \sigma_{\omega 1} = 0.5, \qquad \beta_1 = 0.075, \qquad \beta^* = 0.09$$

$$\kappa = 0.41, \qquad \gamma_1 = \beta_1/\beta^* - \sigma_{\omega 1}\kappa^2/\sqrt{\beta^*}$$

Set 2 (ϕ_2):

$$\sigma_{k_2} = 1.0, \qquad \sigma_{\omega 2} = 0.856, \qquad \beta_2 = 0.0828, \qquad \beta^* = 0.09$$

$$\kappa = 0.41, \qquad \gamma_2 = \beta_{21}/\beta^* - \sigma_{\omega 2}\kappa^2/\sqrt{\beta^*}$$

Set 1 corresponds to the k–ω model that is used in the near-wall region, and set 2 corresponds to the transformed k–ε model that is applied for free shear layers. The eddy viscosity of the baseline model is supplemented by the following relation:

$$\mu_t = \rho(k/\omega) \tag{12}$$

B. SST Model

The SST model was developed to consider the transport of the principal turbulent shear stress, which employed the limitation of the turbulent shear stress that is based on Bradshaw's assumption that the shear stress in the turbulent boundary layer is proportional to the turbulent kinetic energy,

$$\tau_{ij} = a_1\rho k \tag{13}$$

with $a_1 = 0.31$. The shear stress of the turbulence models are also computed from

$$\tau_{ij} = \mu_t\Omega_{ij}, \qquad \Omega_{ij} = \frac{1}{2}\left(\frac{\partial u_i}{\partial x_j} - \frac{\partial u_j}{\partial x_i}\right) \tag{14}$$

where $|\Omega|$ is the absolute value of the vorticity. Within this framework of a conventional eddy-viscosity model, Menter redefined the eddy viscosity as follows:

$$\mu_t = a_1\rho k/|\Omega| \tag{15}$$

which finally provided the expression

$$\mu_t = \frac{a_1\rho k}{\max(a_1\omega, |\Omega|)} \tag{16}$$

which guarantees that the shear stress does not change more rapidly than $\rho a_1 k$ in the adverse pressure gradient region. To recover the original formulation of the BSL for the free shear layers, a blending function was used,

$$\mu_t = \frac{a_1\rho k}{\max(a_1\omega, |\Omega|\boldsymbol{F}_2)} \tag{17}$$

where $\boldsymbol{F}_2$ is defined as follows:

$$\arg_2 = \max\left[\frac{2\sqrt{k}}{0.09\omega y}, \frac{500\mu}{\rho\omega y^2}\right] \tag{18}$$

$$F_2 = \tanh\left(\arg_2^2\right) \tag{19}$$

The constants for the SST model are changed within this relation to give the following two sets of model constants.

Set 1(ϕ_1):

$$\sigma_{k1} = 0.85, \qquad \sigma_{\omega 1} = 0.5, \qquad \beta_1 = 0.075, \qquad \beta^* = 0.09$$

$$\kappa = 0.41, \qquad \gamma_1 = \beta_1/\beta^* - \sigma_{\omega 1}\kappa^2/\sqrt{\beta^*}$$

Set 2 remains the same.

The SST model has provided very accurate results for the simulations of separated flows with an adverse pressure gradient. The prediction of the flowfield with weak SBLI showed an agreement with the experimental data.

C. MSST Model

The SST model has sometimes yielded the overprediction of the separated flow regions where strong SBLIs occur. This is one of the reasons that the SST model was derived for incompressible flow, and the value of a_1 may need to be reevaluated for compressible flows. Another reason is the usage of the absolute value of the vorticity $|\Omega|$ for redefining the shear stress and the eddy viscosity in Eqs. (14) and (15). In the conventional turbulence models, however, the shear stress is proportional to the shear strain rate S_{ij} as follows:

$$\tau_{ij} = \mu_t S_{ij}, \qquad S_{ij} = \frac{1}{2}\left(\frac{\partial u_i}{\partial x_j} + \frac{\partial u_j}{\partial x_i}\right) \tag{20}$$

which is more consistent with the eddy-viscosity assumption in the Reynolds averaged Navier–Stokes equation based on the Boussinesq approximation. In this work, the MSST model adopted this equation instead of Eq. (14) used in the SST model to achieve rotational invariance, which seems to be a sounder measurement of fluid distortion than the vorticity in a complex flowfield. Consequently, the new expression of the eddy viscosity is given by

$$\mu_t = \frac{a_1\rho k}{\max(a_1\omega, |S|\boldsymbol{F}_2)} \tag{21}$$

The model constants and the blending function remains unchanged from those used in the SST model.

III. Numerical Methods

The CSCM upwind flux difference splitting method utilizes the properties of similarity transformation based on the conservative, the primitive, and the characteristic variables,

$$\begin{aligned}\Delta F &= A\Delta q = MT\Lambda T^{-1}M^{-1}\Delta q \\ &= MT\Lambda T^{-1}\Delta\tilde{q} = MA'\Delta\tilde{q} \\ &= MT\Lambda\Delta\tilde{\tilde{q}}\end{aligned} \tag{22}$$

Lambda is a diagonal matrix whose diagonal elements correspond to the eigenvalues $(u, u, u+a, u-a, u, u)$ and variables q, $\tilde{q}$, and $\tilde{\tilde{q}}$ are related as follows:

$$\Delta q = M^{-1}\Delta\tilde{q}, \qquad \Delta\tilde{\tilde{q}} = T^{-1}\Delta\tilde{q} \tag{23}$$

The M matrix transforms the primitive variable difference into the conservative variable difference. T^{-1} is the transformation matrix of the primitive variable difference into the characteristic variable difference, and it is somewhat arbitrary concerning scaling, which leads to logarithmic difference approximations for the density, pressure, and Mach number.

The characteristic variables can be obtained from the primitive variables through the following relation:

$$T^{-1}(A'\Delta\tilde{q}) = T^{-1}(T\Lambda T^{-1})\Delta\tilde{q} = \Lambda\Delta\tilde{\tilde{q}} \tag{24}$$

The inviscid flux $\Delta\boldsymbol{F}$ can be divided into $\Delta\boldsymbol{F}^+$ and $\Delta\boldsymbol{F}^-$ using a diagonal truth function matrix $D^{\pm}$, and Eq. (11) can be written as

$$\Delta\boldsymbol{F} = MT(D^+ + D^-)T^{-1}A'\Delta\tilde{q} = \Delta\boldsymbol{F}^+ + \Delta\boldsymbol{F}^- \tag{25}$$

$$D^+ = \tfrac{1}{2}[1 + (\Lambda/|\Lambda|)], \qquad D^- = \tfrac{1}{2}[1 - (\Lambda/|\Lambda|)] \tag{26}$$

When the relation $A'\Delta\tilde{q} = \tilde{M}^{-1}\Delta q$ is used, Eq. (25) can be rewritten as

$$\Delta \boldsymbol{F}^{\pm} = MTD^{\pm}T^{-1}\tilde{M}^{-1}\Delta q = A^{\pm}\Delta q \tag{27}$$

Equation (27) satisfies the property U of Roe,[12] and thus, the flux vectors are conserved. Although the formulation becomes complicated due to transformation matrices M, T, and $\tilde{M}_i^{-1}$ the differencing scheme in turn has the representation of the convective flow propagation through these matrices and naturally allows easy characteristic boundary conditions via modified T'^{-1}.

The implicit finite difference equation can be discretized using one-side differencing, depending on the sign of eigenvalues of the Jacobian matrices. For third-order accuracy of the inviscid terms in the explicit part (right-hand side), we use the flux extrapolation with the minmod limiter.[17] With use of approximate factorization (Warming and Beam[18]), the equations are solved along the ξ direction and then the η direction successively. We consider that converged solutions are obtained when the $L2$ residual of all variables reaches 1.0×10^{-6}.

IV. Grid System and Boundary Conditions

The grid system was generated by elliptic partial differential equation grid techniques, and a stretching function was used to cluster most grid points near the wall. The grid system was 100×60 over the axisymmetric bump in the longitudinal and normal directions, respectively (Fig. 1a). The same configuration was used experimentally by Johnson et al.[19] The incoming flow properties were prescribed by freestream values. Also, the 110×90 grid system was constructed for the supersonic flow cases of the compression ramp (Fig. 1b). The first grid point is located at $y^+ \approx 1$ away from the wall, and 70 points were contained in the normal direction within the boundary layer on the flat plate. The incoming flow properties were prescribed by using the solutions of the turbulent flat-plate flow. In all cases, a first-order extrapolation was used at outflow boundaries. At the wall surface, the no-slip boundary condition and the adiabatic condition were used. The turbulent kinetic energy was set to zero on the wall, and ω was given by

$$\omega = 10\left[6\mu \Big/ \rho\beta_1(\Delta y_1)^2\right] \tag{28}$$

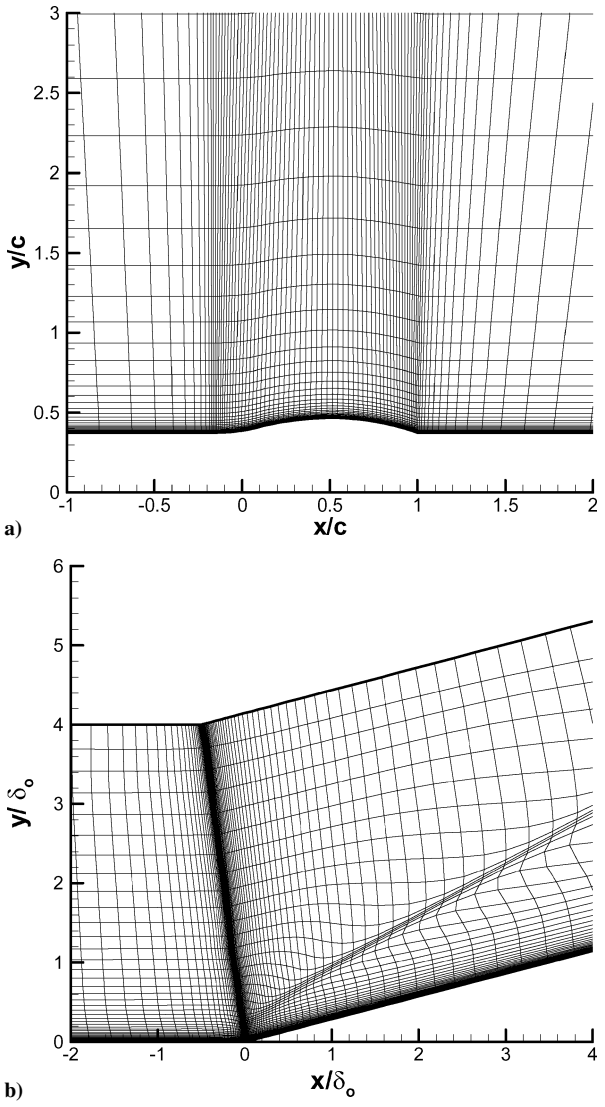

Fig. 1 Grid system for a) bump flow and b) 16-deg compression corner flow.

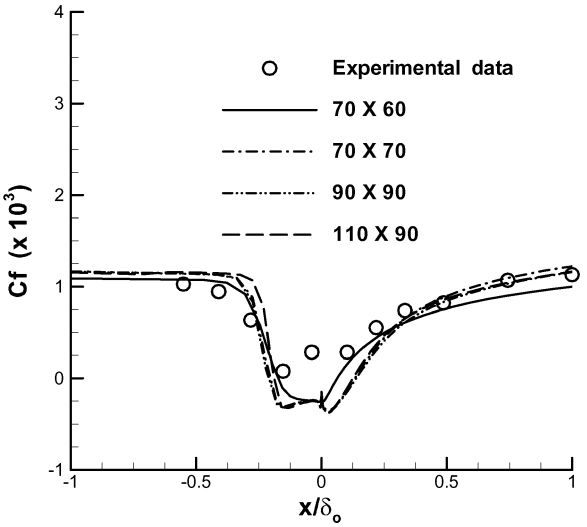

Fig. 2 Dependence of skin-friction coefficient distribution on a number of grid points in a 16-deg compression corner flow.

Figure 2 shows the grid dependence of the skin-friction coefficients for the 16-deg compression corner resulting from the simulation using the BSL model. In the grid-resolution study, the number of grid points was increased by inserting additional grid points on the boundaries. The results indicate that the number of grid points used in the current study was sufficient to resolve the SBLI because little change of the skin-friction coefficient was noted for more grid points in each direction.

V. Results and Discussion

A. Transonic Bump Flow

The transonic, axisymmetric bump flow with weak SBLI was used in the evaluations of the turbulence models. The freestream Mach number was 0.875 and the Reynolds number based on the length of the bump was 2.761×10^6. The general characteristics of the axisymmetric turbulent flowfield over the bump were compared with the experimental data of Johnson et al.[19] and the results from three different turbulence models. Figures 3a and 3b result from the current numerical simulation by the BSL model. Figure 3a shows the dimensionless pressure contours in the flowfield around the bump. We can see that the flow acceleration near the front portion of the bump was followed by a weak shock occurring on the latter portion of the bump, which was clearly predicted by the current numerical method. After the transonic shock/turbulent boundary-layer interaction, the velocity profile was suddenly distorted and detached by the adverse pressure gradient. The diverged geometric effect is shown in Fig. 3b.

Figure 4 shows the dimensionless surface pressure distribution along the wall surface of the bump. The wall pressure values of each model are identical to each other until the compression wave is encountered at about $x/c = 0.5$. Because of the acceleration of the flow, which reaches to the low supersonic flow downstream of bump leading edge, the pressure decreases almost linearly, until the weak shock occurs. Then, the pressure increases sharply after

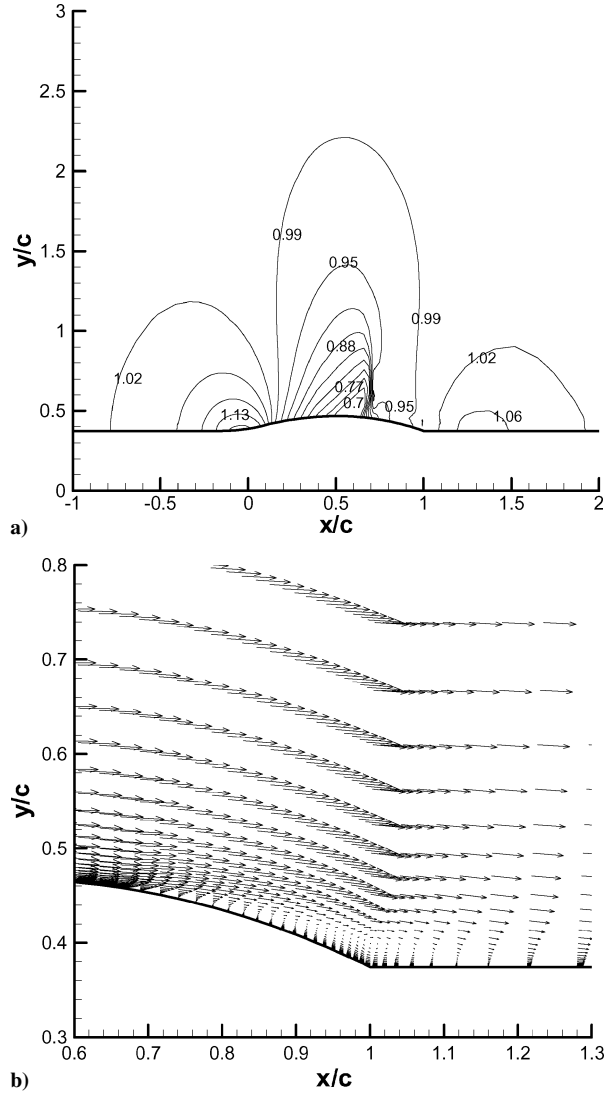

Fig. 3 Simulation results of a transonic bump flow: a) nondimensional static pressure contours and b) velocity vectors near the end of the bump.

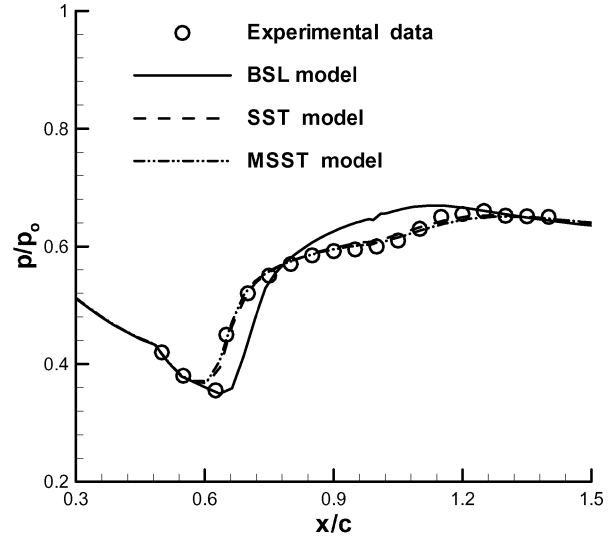

Fig. 4 Nondimensional pressure distribution on the wall surface of the bump.

the weak shock at about $x/c = 0.6$. The experimental data show a small plateau of pressure distribution near $x/c = 1$, partly due to the flow separation downstream of the transonic SBLI. When the mean flowfield is suddenly distorted due to the shock, the conventional two-equation turbulence models tend to yield a sudden increase in the Reynolds shear stress and the eddy-viscosity level, which rarely produces the separated flow caused by the weak SBLI and adverse pressure gradient. That is why models such as the BSL model might have some deficiencies in predicting the pressure distribution around the flow separation region. However, the SST model was derived to prevent the shear stress from increasing rapidly, and it shows good performance in predicting the pressure distribution on the bump wall surface around the flow separation region. The wall pressure distributions of the MSST model proposed herein were identical to those of the SST model, although the BSL model could not show the plateau of the wall pressure distributions.

B. Supersonic Compression Ramp

The BSL, SST, and MSST models were applied to the compression corner cases with the strong shock/turbulent boundary-layer interaction. The freestream Mach number was 2.85, and three different ramp angles were 16, 20, and 24 deg. The experiments of Settles et al.[1] deal with the two-dimensional ramp placed on the bottom wall of a wind tunnel to allow the shock to occur, which interferes with the turbulent boundary layer. Figure 5a shows the dimensionless

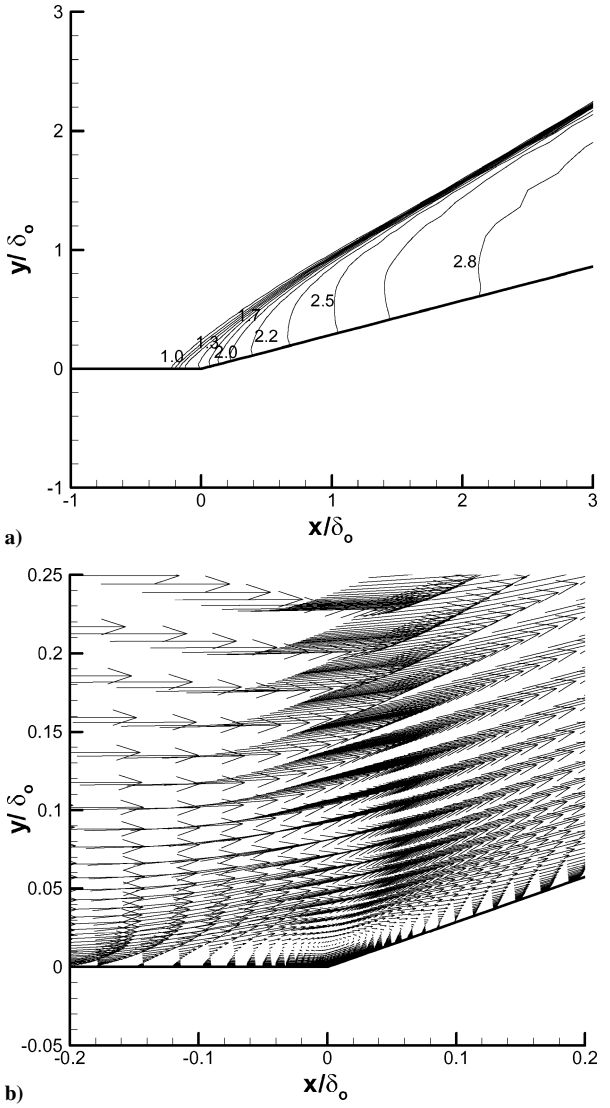

Fig. 5 Simulation results of a supersonic ramp flow: a) nondimensional static pressure contours and b) velocity vectors near the end of the bump.

pressure contours over the 16-deg compression ramp. The shock was clearly predicted with the shock angle of 37 deg, which corresponds to the oblique shock relations with a deflection angle of 16 deg. After the shock occurs, the sharp increase in static pressure and the direction change of the boundary-layer flow cause the turbulent boundary layer to thicken just upstream of the corner. The incipient flow separation was found in the 16-deg ramp flow (Fig. 5b).

Figure 6a shows the surface pressure distribution along the wall of the 16-deg compression ramp. The wall pressure is identical to the freestream value until the oblique shock occurs at about $x/\delta_0 = -0.3$. The pressure gradient decreased downstream of the corner, and the pressure eventually reached a level of theoretical inviscid pressure rise, as expected. The SST and MSST model exhibited a small kink near the corner, indicating the presence of flow separation. All models are highly consistent with the experimental data. The skin-friction coefficient distribution along the wall surface is shown in Fig. 6b. The skin-friction coefficients from the BSL, SST, and MSST models are in reasonably good agreement with the experimental data in the forward portion of the sharply decreasing skin-friction coefficient. However, all of the models failed to predict the skin-friction values in the separated flow region, although all of the models produce a good rate of skin-friction coefficient recovery downstream of the shock on the inclined wall surface.

For the 20-deg ramp (Fig. 7a), the difference of the prediction performance among models began to be revealed clearly. Even though

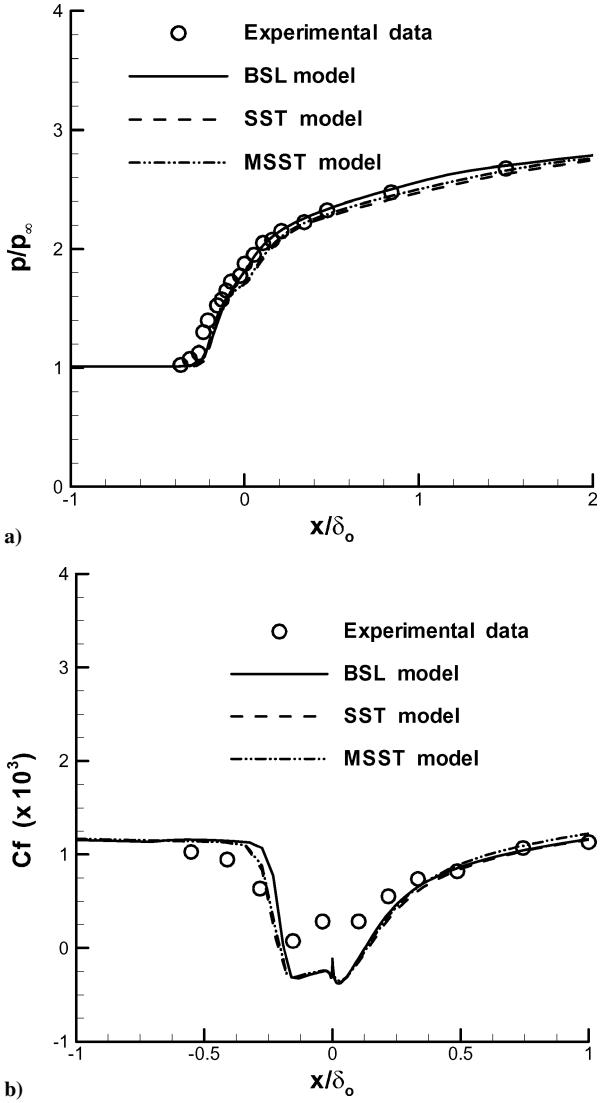

Fig. 6 Simulation results of a 16-deg compression corner flow: a) nondimensional wall pressure and b) skin-friction coefficient distributions.

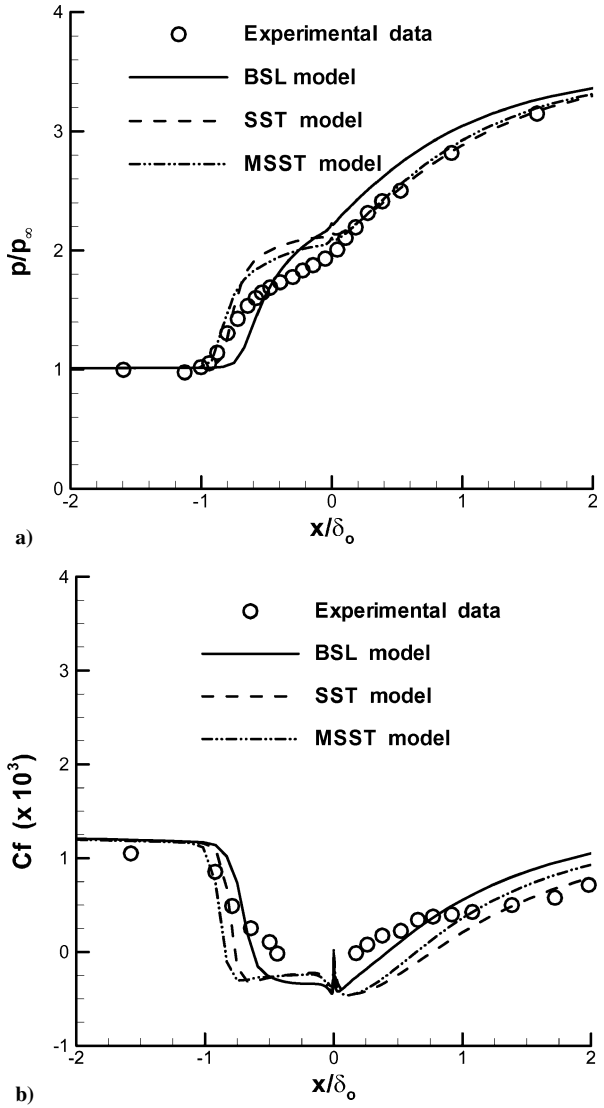

Fig. 7 Simulation results of a 20-deg compression corner flow: a) nondimensional wall pressure and b) skin-friction coefficient distributions.

the SST and MSST models overpredict the wall pressure rise within the flow separation region, these models show an agreement of the wall pressure distribution with the experimental data downstream of the redeveloped region. The BSL model underpredicts the shock location and shows the rapid increase of the wall pressure after the shock. All of the models overpredict the separation bubble sizes and produce the reattachment points farther downstream than the experiment because these models fail to yield the rapid recovery of the boundary layer downstream of the shock (Fig. 7b). For the velocity profile comparisons shown in Fig. 8, the differences among the results obtained using theses models are shown only where the results show some disagreement with the experimental data around the separated flow region. Unlike the BSL model, the MSST and SST models show that the velocity profiles are easily distorted and yield a good comparison with the experimental results immediately downstream of shock location (Fig. 8b). All of the computed velocity profiles are in substantial disagreement with the experimental data in the recovery region downstream of the corner (Fig. 8d).

For the 24-deg ramp, the normalized wall pressure and the skin-friction coefficient distributions are compared in Fig. 9. Experimental results indicated that the shock structure may experience unsteady oscillations and three dimensionality of the flow. The steady two-dimensional assumption may have deteriorated the computational results in this case.[1] The MSST model, however, shows good agreement with the shock location and the wall pressure rise in the flow recovery region downstream of the SBLI, even

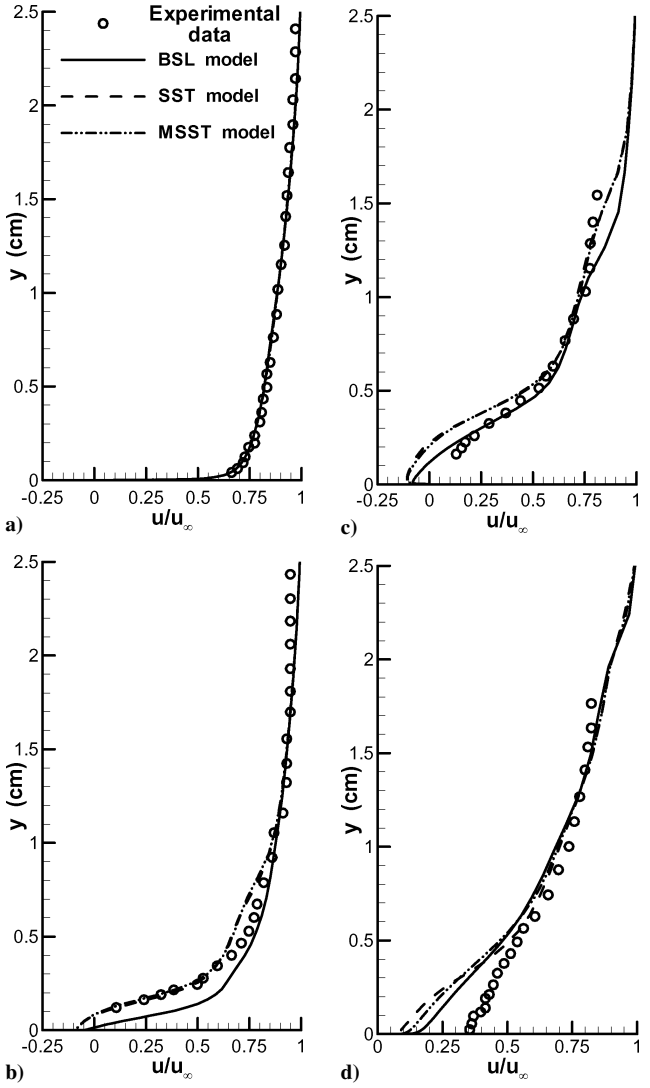

Fig. 8 Predicted mean velocity profiles compared with the experimental data of Settles et al.[1] for a 20-deg compression corner flow: a) $x/\delta_0 = -1.60$, b) $x/\delta_0 = -0.47$, c) $x/\delta_0 = 0.0$, and d) $x/\delta_0 = 1.06$.

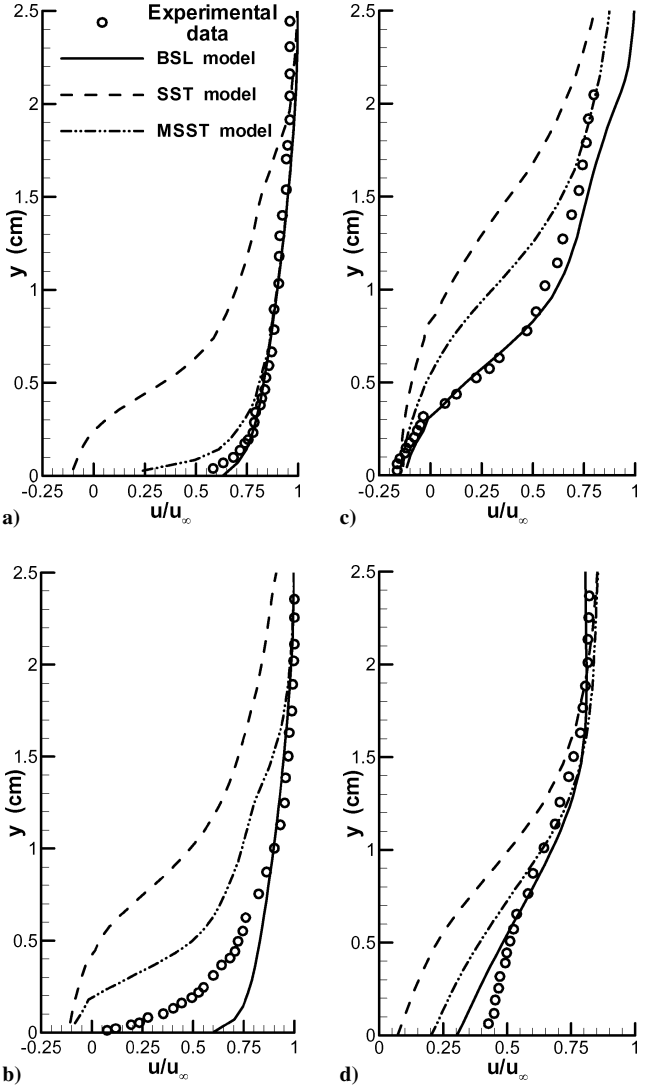

Fig. 10 Predicted mean velocity profiles compared with the experimental data of Settles et al.[1] for a 24-deg compression corner flow: a) $x/\delta_0 = -2.17$, b) $x/\delta_0 = -1.48$, c) $x/\delta_0 = 0.0$, and d) $x/\delta_0 = 2.89$.

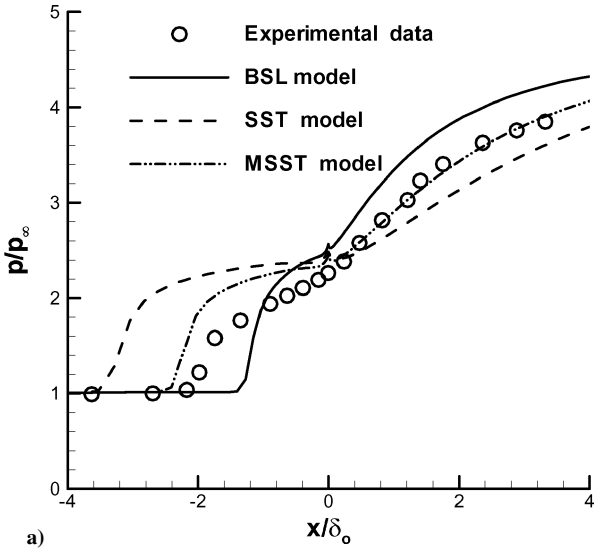

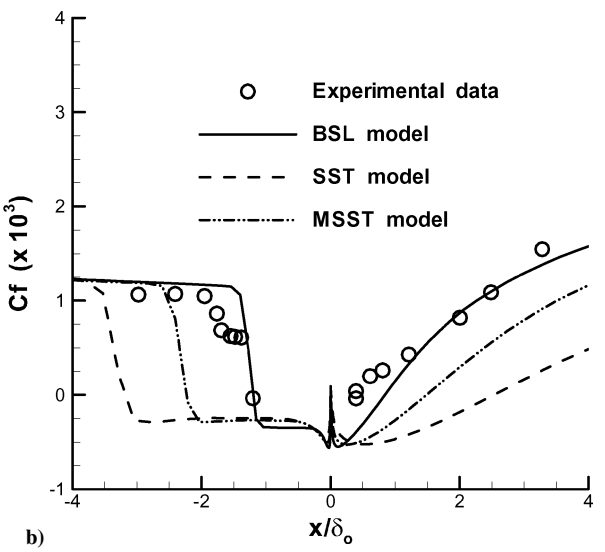

Fig. 9 Simulation results of a 24-deg compression corner flow: a) nondimensional wall pressure and b) skin-friction coefficient distributions.

though the BSL and SST models yield a severe discrepancy in those predictions. The SST model shows very low skin-friction coefficient distribution downstream of the SBLI, but the MSST model produces a more accurate prediction in the redevelopment region (Fig. 9b).

Comparisons of the mean velocity profiles at several locations along the wall surface of the 24-deg ramp, are shown in Fig. 10. Upstream of the shock, $x/\delta_0 = -2.17$, the computed result from the BSL model was found to be similar to that obtained experimentally, even though the SST model predicted flow reversal. The BSL model, however, still showed a fully developed velocity profile downstream of the shock, $x/\delta_0 = -1.48$, whereas the experimental data showed a defected velocity profile due to the SBLI. The MSST model predicted a smaller discrepancy from the experimental data in the severe reversed flow region than the SST model did (Fig. 10c). All models showed that the redevelopment of the boundary layer was somewhat slow downstream of the reattachment portion and especially showed some deviation of the velocity profiles from the experimental data near the wall region.

VI. Conclusions

The BSL and the SST models of Menter and the MSST model proposed here were used to predict transonic/supersonic compressible flows, including SPLI. For the modification of SST model, the absolute value of the vorticity tensor was replaced by the scalar measurement of the shear strain rate to achieve rotational invariance.

In the case of a transonic axisymmetric flow with the weak SBLI, the wall pressure distribution yielded by the MSST model was identical to that of the SST and bill models agreed with the experimental data, although the BSL model did not show the plateau of the wall pressure distributions near the end of the bump. In a 16-deg ramp flow, all of the models produced a good rate of skin-friction coefficient recovery and wall pressure distribution downstream of the shock. In the cases of the 20- and 24-deg compression corners, which imply strong SBLI, the MSST model resulted in a more accurate prediction of the shock location and the wall pressure distribution in the flow recovery region downstream of the shock. It also produced more reasonable mean velocity profiles, separation bubble sizes around the reversed flow zones, and skin-friction coefficient distributions in the redevelopment regions, as compared to the SST model. The performance evaluations in the current numerical simulations indicated the enhanced capability of the MSST model proposed here to predict the adverse pressure gradient flow of the compression ramps with strong SBLI.

Acknowledgment

This work was supported by the Brain Korea 21 project and a Grant No. R08-2004-000-10556-0 from Korea Science and Engineering.

References

[1]Settles, G. S., Fitzpatrick, T. J., and Bogdonoff, S. M., "Detailed Study of Attached and Separated Compression Corner Flowfields in High Reynolds Number Supersonic Flow," *AIAA Journal*, Vol. 17, No. 6, 1979, pp. 579–585.

[2]Visbal, M., and Knight, D., "The Baldwin–Lomax Turbulence Model for Two-Dimensional Shock-Wave/Boundary-Layer Interactions," *AIAA Journal*, Vol. 22, No. 7, 1984, pp. 921–928.

[3]Wilcox, D. C., "Comparison of Two-Equation Turbulence Models for Boundary Layers with Pressure Gradient," *AIAA Journal*, Vol. 31, No. 8, 1993, pp. 1414–1421.

[4]Forsythe, J. R., Hoffmann, K., and Damevin H. M., "An Assessment of Several Turbulence Models for Supersonic Compression Ramp Flow," AIAA Paper 98-2648, June 1998.

[5]Zheltovodov, A. A., "Shock Waves/Turbulent Boundary-Layer Interactions—Fundamental Studies and Applications," AIAA Paper 96-1977, Jan. 1996.

[6]Baldwin, B. S., and Lomax, H., "Thin Layer Approximation and Algebraic Model for Separated Turbulent Flows," AIAA Paper 78-257, Jan. 1978.

[7]Menter, F. R., "Influence of Freestream Values on k–ω Turbulence Model Predictions,"*AIAA Journal*, Vol. 30, No. 6, 1991, pp. 1657–1659.

[8]Menter, F. R., "Two-Equation Eddy-Viscosity Turbulence Models for Engineering Applications," *AIAA Journal*, Vol. 32, No. 6, 1994, pp. 1598–1605.

[9]Steger, J. L., and Warming, R. F., "Flux Vector Splitting of the Inviscid Gasdynamics Equations with Application to Finite Difference Methods," *Journal Computational Physics*, Vol. 40, 1981, pp. 263–293.

[10]Van Leer, B., "Flux-Vector Splitting for Euler Equations," *Proceedings of the 8th International Conference on Numerical Methods in Fluid Dynamics*, Lecture Notes in Physics, Vol. 170, Springer-Verlag, Berlin, 1982, pp. 507–512.

[11]Godunov, S. K., "A Finite Difference Method for the Numerical Computation of Discontinuous Solutions of the Equations of Fluid Dynamics," *Mat. Sbornik*, Vol. 47, 1959, pp. 357–393.

[12]Roe, P. L., "The Use of the Riemann Problem in Finite-Difference Schemes," *Proceedings of the 7th International Conference on Numerical Methods in Fluid Dynamics*, Lecture Notes in Physics, Vol. 141, Springer-Verlag, Berlin, 1981, pp. 354–359.

[13]Osher, S., "Riemann Solvers, the Entropy Condition, and Difference Approximations," *SIAM Journal on Numerical Analysis*, Vol. 21, No. 2, 1984, pp. 217–235.

[14]Lombard, C. K., Bardina, J., Venkatapathy, E., and Oliger, J., "Multi-dimensional Formulation of CSCM—An Upwind Flux Difference Eigenvector Split Method for the Compressible Navier–Stokes Equations," AIAA Paper 83-1859CP, 1983.

[15]Kim, S. D., Kwon, C. O., and Song, D. J., "Comparison of Turbulence Models in Shock–Boundary Layer Interaction," *KSME International Journal*, Vol. 18, No. 1, 2004, pp. 153–166.

[16]Song, D. J., Kim, S. D., Kwon, C. O., and Seo, J. I., "A Computational Off-Design Performance Analysis of Centrifugal Compressor Diffusers," *Computational Fluid Dynamics Journal*, Vol. 6, No. 4, 1998, pp. 549–560.

[17]Hirsch, C., Numerical Computation of Internal and External Flows, Vol. 2, Wiley, New York, 1989, pp. 493–594.

[18]Warming, R. F., and Beam, R. M., "On Construction and Application of Implicit Factored Schemes for Conservation Laws," *SIAM–AMS Proceedings*, American Mathematical Society, Providence, RI, Vol. 11, No. 2, 1977, pp. 85–129.

[19]Johnson, D. A., Horstman, C. C., and Bachalo, W. D., "Comparison Between Experiment and Prediction for a Transonic Turbulent Separated Flow," *AIAA Journal*, Vol. 20, No. 7, 1982, pp. 737–744.